Combining viscoelastic damping and nonlinearities to widen the operational speed range of flutter energy harvesting

Marcelo A. Delgado Filho[1]
André G. Cunha Filho
Antônio M. G. de Lima
Structural Mechanics Laboratory - LMEst,
School of Mechanical Engineering,
Federal University of Uberlândia,
Av. João Naves de Ávila, 2121,
Uberlândia, MG 38408-100, Brazil
email: marcelo.delgado@ufu.br

Noureddine Bouhaddi
Najib Kacem
Université Marie et Louis Pasteur, CNRS,
institut FEMTO-ST, F-25000 Besançon,
France

We propose using viscoelastic damping with combined hardening and free-play structural nonlinearities to enhance energy harvesting performance and control vibration in a pitch and plunge airfoil with piezoelectric transduction. Numerical simulations are performed by directly integrating the equation of motion in the time domain under unsteady aerodynamic load. In addition, a fractional derivative model efficiently accounts for the behavior of the viscoelastic material. This study analyzes the effect of each structural nonlinearity and identifies a good condition for harvesting in terms of cut-in speed and operational speed range. For this condition, the viscoelastic damper in pitch can further reduce the cut-in speed by 13 *%, slightly increase the harvested power, and help reduce the dynamical complexity of the system response. In turn, the viscoelastic damper in the plunge degree of freedom can control the vibration amplitude at post-critical flow speeds, increasing the operational speed range up to* 28 *% and the power up to two orders of magnitude in some cases. Viscoelastic damping maintains a favorable harvesting condition for temperature variations from* 10°C *to* 35°C.

Keywords: Flutter energy harvesting, Passive control, Viscoelasticity, Nonlinear aeroelasticity

1 Introduction

With the rise of the Internet of Things and Industry 4.0, wireless sensors and small-scale electronic devices are becoming increasingly widespread [1]. However, because they traditionally rely on batteries, their deployment may be impractical in some cases, especially in remote or hard-to-access areas [2]. In addition, battery replacement is a costly and time-consuming task [1] that creates chemical waste requiring special processing. Therefore, researchers and engineers have proposed new power generation strategies. Through energy harvesting, it is possible to convert different readily available energy sources such as wind, solar, thermal, light, and kinetic into electrical power [3]. The latter is an encouraging possibility, as it has a high power density and is widely available in the form of mechanical vibrations [4]. Flow-subjected structures are prone to oscillate in the form of aeroelastic-induced vibration. The phenomena include vibrations induced by vortex and wake, galloping, and flutter, all of which can be used for harvesting [5]. Flutter-driven energy harvesters can achieve large structural deformations resulting in high output voltage [6]. Furthermore, they are suitable for many environments and have a low cut-in speed [2], meaning the minimum airspeed necessary to achieve energy harvesting.

Flutter is an aeroelastic phenomenon in which the interaction with the flow changes the stiffness and damping of the system at each flow speed, causing the structure to extract energy from the flow as one of the vibration modes becomes negatively damped [7]. For a linear aeroelastic system, the response grows indefinitely upon increasing the airspeed after reaching the neutral stability condition at the

[1]Corresponding Author.
Version 1.18, March 10, 2025

critical flutter speed, representing a substantial drawback of linear harvesters. This limitation can be overcome by including nonlinearities since they originate persistent power in the form of Limit Cycle Oscillations (LCO) before and after the critical speed [8], increasing the range of operational flow speeds of the harvester as a result [9]. Therefore, incorporating nonlinearities is essential to assess the full potential of the energy harvesting system.

The classical pitch and plunge airfoil can limit the complexity of the aeroelastic system in the presence of nonlinearities while providing a reasonable insight into the dynamic behavior [10,11]. Thus, the pitch and plunge airfoil has been selected by many researchers when incorporating nonlinearities in flutter energy harvesting. The authors who first proposed flutter to harvest power, Ref. [12,13], made a further contribution by considering the nonlinear effect of dynamic stall for a beam connected to a flap while performing experimental tests [14]. The study offers design recommendations based on whether the flow condition was variable or constant. By combining free play with hardening nonlinearities in pitch degree of freedom (dof), Ref. [15] concluded that the former reduced the cut-in speed while the latter could contribute to the control of the LCO in the post-flutter, therefore increasing the operational speed range of the harvester. Ref. [16] examined cubic hardening nonlinearities in pitch and plunge springs of a two-DOF airfoil, finding that the pitch spring has the most significant influence on the system. The study also showed that while electrical load resistance affects voltage and power output, it has little impact on pitch and plunge motions or flutter speed. Ref. [17] demonstrated recently that an airfoil with an unconstrained flap could alternate between the flutter and the vortex energy harvesting mechanisms, depending on the flap damping coefficient.

References [18,19] proposed multi-segmented nonlinearities to control the LCO. Reference [20] used a nonlinear energy sink and an energy harvester to control the nonlinear response of a plate in the hypersonic regime. Another option to control the LCO may be the use of viscoelastic materials. These have been successfully proposed for flutter suppression of both plates in the supersonic regime [21,22] and of for pitch and plunge airfoils in the subsonic regime [23,24]. When applying a hybrid control to a two-dof airfoil, Ref. [24] found that the passive viscoelastic approach alone was responsible for most of the gain. Sliding mode control was effective in vibration suppression of a harmonically excited viscoelastic airfoil [25]. A visco-hysteretic vibration absorber was proposed for the suppression of flutter [26]. In turn, Ref. [27] investigated the influence of random fluctuations on a two-dof airfoil with viscoelastic terms under steady aerodynamics. They found that random fluctuations can induce stochastic jumps and that the viscoelastic material meaningfully influences the airfoil behavior. Reference [28] studied a three-dof typical section with hardening nonlinearities in the pitch and flap dofs, showing that viscoelastic damping can reduce the LCO amplitudes and increase the flutter speed. Ref. [29] demonstrated the same for a three-dof typical section with free-play and a rotational viscoelastic damper on the control surface.

Viscoelastic damping may be an alternative way of tuning the harvester performance, given that the viscoelastic material allows for the convenient incorporation of stiffness and damping with a single element. As shown in the literature [15,16,30,31], the relationship of stiffness and damping with the harvested power in nonlinear aeroelastic systems is non-monotonic, such that incrementing either damping or stiffness may increase the power output. Hence, stiffness and damping are key factors for harvester performance. Moreover, as viscoelastic damping is a passive technique, none of the power harvested is spent with control actuation. Therefore, this paper evaluates the use of viscoelastic dampers combined with hardening and free-play nonlinearities to control the LCO amplitude and improve the performance of a piezoelectric flutter energy harvesting (FEH) device. To the best of the authors' knowledge, this approach is unprecedented in existing research, representing a new contribution to the wind energy harvesting field. In addition, a recurrent fractional derivative method is applied to this problem for the first time, enabling efficient analysis in the time domain. Reference [32]

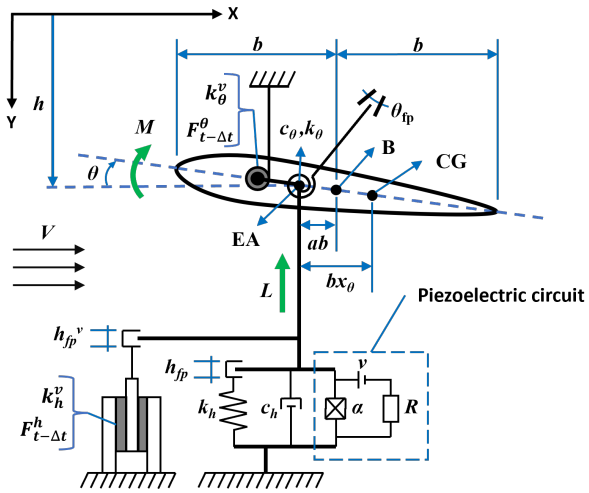

Fig. 1 Two-dof energy harvesting airfoil with viscoelastic dampers and nonlinear springs.

reported a gain superior to 98 % in computation time when using this method. The possibility of working in the time domain allows the observation of the complex dynamics of the nonlinear FEH device with viscoelastic damping, marking an advancement in the area.

First, section 2 describes the nonlinear piezoaeroelastic system, including the fractional derivative formulation of the viscoelastic material. Section 3 addresses the influence of the combined nonlinearities and suggests a favorable configuration for harvesting from the hardening and free-play combined nonlinearities. The viscoelastic damping is applied to this configuration in section 4, on the pitch and plunge dofs, and section 5 presents the conclusions.

2 Nonlinear piezoaeroelastic model with viscoelastic damping

As previously stated, the well-known two-dof typical section can give a reasonable physical representation of aeroelastic phenomena while restricting the analysis complexity when dealing with nonlinearities [10,11]. The typical section has pitch θ and plunge h degrees of freedom (dof) , interacting with an inviscid and incompressible flow of speed V (Fig. 1). h is measured on the elastic axis (EA) and is positive downward, while θ is positive nose up. The dashed rectangle highlights the energy harvesting circuit. As can be seen, the piezoelectric coupling is in the plunge dof, and the electric resistance R dissipates the voltage output v. Thus, as the flow excites the system, the direct piezoelectric effect converts part of the vibration energy associated with h into electrical power.

The extended Hamilton principle yields the equation of motion [33], leading to Eq. (1), where $\bar{m}$ is the total mass of the airfoil and its support; m is the mass of the airfoil alone; b is the semi-chord; $I = mr_\theta^2$ is the moment of inertia around EA with r_θ being the radius of gyration; $c_{h,\theta}$ and $k_{h,\theta}^{nl}$ are respectively the viscous structural damping and nonlinear stiffness terms associated with h and θ. B is a reference point at b, from which the dimensionless parameter a specifies the EA location. Moreover, x_θ is the chord-wise offset between the reference point at the EA and the center of gravity CG, also dimensionless. Finally, L is the lift force, and M is the momentum about the EA, both given per unit length of the span l. As a result of electromechanical coupling α, the voltage dof appears in Eq. (1). Therefore, one more differential equation is necessary to fully describe the system, which is given by Eq. (2), where C_{eq} is the equivalent capacitance of the piezoceramic layer.

$$\begin{pmatrix} \bar{m} & mx_\theta \\ mx_\theta & I \end{pmatrix}\begin{pmatrix} \ddot{h} \\ \ddot{\alpha} \end{pmatrix}+\begin{pmatrix} c_h & 0 \\ 0 & c_\alpha \end{pmatrix}\begin{pmatrix} \dot{h} \\ \dot{\alpha} \end{pmatrix} +\begin{pmatrix} {k_h}^{nl} & 0 \\ 0 & {k_\alpha}^{nl} \end{pmatrix}\begin{pmatrix} h \\ \alpha \end{pmatrix}-\begin{pmatrix} \alpha v \\ 0 \end{pmatrix}=l\begin{pmatrix} -L \\ M \end{pmatrix} \tag{1}$$

$$C_{eq}\dot{v}+v/R\ +\alpha\dot{h}=0 \tag{2}$$

In the proposed work, hardening-type nonlinearity is combined with free-play in the discontinuous fashion as given by:

$$k_x^{nl}=\begin{cases} \frac{k_x^l}{x}\left(a_0^x\left(x-x_{fp}\right)+a_1^x\left(x-x_{fp}\right)^3\right) & x>x_{fp} \\ 0 & -x_{fp}\le x\le x_{fp} \\ \frac{k_x^l}{x}\left(a_0^x\left(x+x_{fp}\right)+a_1^x\left(x+x_{fp}\right)^3\right) & x<-x_{fp} \end{cases} \tag{3}$$

where x represents either h or θ such that x_{fp} denotes the total free-play gap in plunge (h_{fp}) or pitch (θ_{fp}), respectively. The term k_x^l is the linear stiffness. For plunge, $k_h^l=\bar{m}\omega_h^2$, and for pitch $k_\theta^l=I\omega_\theta^2$. ω_h and ω_θ are the uncoupled natural frequencies of plunge and pitch, respectively. It is worth mentioning that a_1^h and a_1^θ are coefficients used to control the hardening intensity. For the linear case, $a_0^h=a_0^\theta=1$ and $a_1^h=a_1^\theta=0$.

The unsteady aerodynamic load is described by thin airfoil theory [34], assuming a bi-dimensional incompressible potential flow. Using the Duhamel formulation [35] and an approximation for the Wagner function, it is possible to simulate arbitrary motion of the airfoil [36]. Following this approach, employing the Jones approximation, the lift L and moment M are represented by:

$$\begin{aligned} L=&\pi b^2\rho\left(\ddot{h}+V\dot{\theta}-ba\ddot{\theta}\right) \\ &+2\pi\rho Vb\left(Q+\chi_1+\chi_2\right) \end{aligned} \tag{4}$$

$$\begin{aligned} M=&\pi b^2\rho\left(V\dot{h}+ba\ddot{h}+V^2\theta-b^2\left(\tfrac{1}{8}+a^2\right)\ddot{\theta}\right) \\ &-\pi\rho Vb^2Q+b\left(a+\tfrac{1}{2}\right)2\pi\rho Vb\left(Q+\chi_1+\chi_2\right) \end{aligned} \tag{5}$$

where $Q=V\theta+\dot{h}+b\left(0.5-a\right)\dot{\theta}$ is the downwash at three quarters of the chord and χ_1 and χ_2 are augmented aerodynamic states. The following expression defines these terms:

$$\begin{pmatrix} \dot{\chi}_1 \\ \dot{\chi}_2 \end{pmatrix}=\begin{pmatrix} -0.041\left(\frac{V}{b}\chi_1\right)-0.165\dot{Q} \\ -0.032\left(\frac{V}{b}\chi_2\right)-0.335\dot{Q} \end{pmatrix} \tag{6}$$

By writing Eq. (4), Eq. (5) and Eq. (6) in matrix form and combining with Eq. (1) and Eq. (2) it is possible to create the following

system of equations:

$$\begin{pmatrix} \tilde{\boldsymbol{M}} & \mathbf{0} & \mathbf{0} \\ -\boldsymbol{b}_1 & \mathbf{0} & \mathbf{0} \\ \mathbf{0} & \mathbf{0} & 0 \end{pmatrix} \ddot{\mathbf{q}} + \begin{pmatrix} \tilde{\boldsymbol{C}} & \mathbf{0} & \mathbf{0} \\ -\boldsymbol{b}_2 & \boldsymbol{I} & \mathbf{0} \\ \mathbf{H} & \mathbf{0} & C_{eq} \end{pmatrix} \dot{\mathbf{q}} + \begin{pmatrix} \tilde{\boldsymbol{K}} & -\boldsymbol{a}_4 & \mathbf{H}^{\mathrm{T}} \\ -\boldsymbol{b}_3 & -\boldsymbol{b}_4 & \mathbf{0} \\ \mathbf{0} & \mathbf{0} & R^{-1} \end{pmatrix} \mathbf{q} = \mathbf{0} \tag{7}$$

where: $\tilde{\boldsymbol{M}} = \begin{pmatrix} \bar{m} & mx_\theta \\ mx_\theta & I \end{pmatrix} - \boldsymbol{a}_1$, $\tilde{\boldsymbol{C}} = \begin{pmatrix} c_h & 0 \\ 0 & c_\theta \end{pmatrix} - \boldsymbol{a}_2$, $\tilde{\boldsymbol{K}}^{\boldsymbol{nl}} = \begin{pmatrix} k_h^{nl} & 0 \\ 0 & k_\theta^{nl} \end{pmatrix} - \boldsymbol{a}_3$, $\mathbf{H} = \begin{pmatrix} \alpha & 0 \end{pmatrix}$ and $\mathbf{q} = \begin{pmatrix} h & \theta & \chi_1 & \chi_2 & v \end{pmatrix}^{\mathrm{T}}$. Appendix A provides the matrices $\boldsymbol{a_j}$ and $\boldsymbol{b_j}$.

The proposed viscoelastic damping consists of the incorporation of two discrete elements, as illustrated by Fig. 1. The component in pitch is a cylindrical segment of angular perimeter Θ, height l_x, and thickness $l_z = R_e - R_i$, where R_e and R_i are respectively the external e internal radii (Fig. 2). In this setup, the viscoelastic material is between the shaft connected to the airfoil and a fixed surface. A layer of dimensions l_x X l_y X l_z made of viscoelastic material interacts with the plunge dof only after a given displacement h_{fp}^v is exceeded (Fig. 2). This amount is indeed a free-play nonlinearity combined with the viscoelastic damping, represented in a discontinuous fashion by the following equation:

$$k_{h,fp}^v = \begin{cases} \frac{k_h^v}{h} & h > h_{fp} \\ 0 & -h_{fp} \leq h \leq h_{fp} \\ \frac{k_h^v}{h} & h < -h_{fp} \end{cases} \tag{8}$$

where k_h^v is the stiffness of the viscoelastic element in plunge.

The two viscoelastic elements work in shear. To model the stress-strain relationship, a fractional derivative method (FDM) is employed (Eq. (9)) as this type of approach allows for more accurate modeling of viscoelastic damping and of the system memory at the cost of a generally higher computation time [32]. To address this inconvenience, [32] proposed a recurrence term that eliminates the stress self-dependency, increasing simulation performance. This aspect is relevant because evaluating the system's nonlinear response involves numerically integrating the equation of motion at several discrete flow speeds until each reaches a steady state. In Eq. (9), G is the shear modulus at low frequency, ξ is the fractional order of the time derivative, and γ_1 and γ_2 are curve fitting coefficients. All these quantities are temperature-dependent and determined from experimental data. The values used here are in Table 1, which was obtained by [32] for the 3M-ISD112, a viscoelastic material manufactured by 3M™. More values are available in the aforementioned source. Since the objective was to characterize the behavior of the viscoelastic damping globally, this study only considered the minimum, maximum, and intermediate available temperatures.

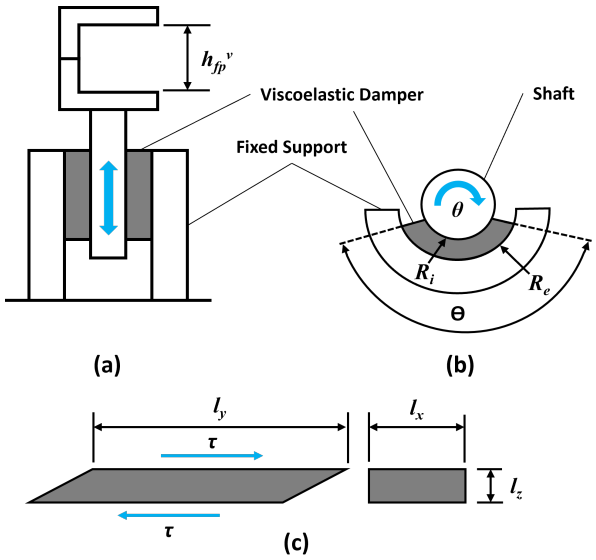

Fig. 2 Plunge viscoelastic element (a), pitch viscoelastic element (b) and viscoelastic element in shear (c).

Table 1 FDM parameters for the considered temperatures [32]

T_v(°C)	G(Pa)	γ_1(Pa·s)	γ_2(s)	ξ(unit: 1)
10	412,887	147,864	$8.217 \cdot 10^{-4}$	0.66714
20	419,582	57,563	$3.162 \cdot 10^{-4}$	0.66780
35	429, 484	16,272	$1.302 \cdot 10^{-4}$	0.67902

$$\tau_t + \gamma_2 \frac{d^{\xi} \tau_t}{dt^{\xi}} = 2G\varepsilon_t + \gamma_1 \frac{d^{\xi} 2\varepsilon_t}{dt^{\xi}} \tag{9}$$

Following the methodology referred to, the Grünwald-Letnikov approximation Eq. (10) represents the fractional derivative [37] of the shear constitutive law, Eq. (9).

$$\frac{d^{\xi} f(t)}{dt^{\xi}} = \Delta t^{-\xi} \sum_{j=0}^{N_l} A_{j+1}^{\xi} f(t - j\Delta t) \tag{10}$$

where $A_{j+1} = \frac{j-\xi-1}{j} A_j$, with $A_1 = 1$, are the Grünwald coefficients, which are straightforward to implement numerically. Next, as proposed by [32], the stress τ_t at a time t is related to a strain history $\epsilon_{t-j\Delta t}$ by Eq. (11), where $N_l = N \cdot \Delta t$ is the memory size given several discrete points N and a time step Δt. The stress in Eq. (11) is no longer self-dependent.

$$\tau_t = \sum_{j=0}^{N_l} \beta_{j+1} \varepsilon_{t-j\Delta t} \tag{11}$$

The so-called recurrent term β_{j+1} is given by:

$$\beta_{j+1} = D_3 A_{j+1} + \sum_{i=0}^{j} D_1 A_{i+1} \beta_{j+1-i} \tag{12}$$

where, from the recurrence formulation, $D_1 = -\frac{\gamma_2 \Delta t^{-\xi}}{1+\gamma_2 \Delta t^{-\xi}}$ and $D_3 = \frac{2\gamma_1 \Delta t^{-\xi}}{1+\gamma_2 \Delta t^{-\xi}}$. Finally, the first term of the recurrence is defined by: $\beta_1 = D_2 = \frac{2G+2\gamma_1 \Delta t^{-\xi}}{1+\gamma_2 \Delta t^{-\xi}}$.

Once the stress-strain relationship has been established, through computing the deformation energy $U = \frac{1}{2}\int \varepsilon \tau d\tilde{V}$ for the viscoelastic elements in pitch and plunge their associated stiffness and dissipative efforts are given respectively by:

$$\begin{pmatrix} {k_h}^v & 0 \\ 0 & {k_\theta}^v \end{pmatrix} = \begin{pmatrix} p_h \beta_1 & 0 \\ 0 & p_\theta \beta_1 \end{pmatrix} \tag{13}$$

$$\begin{pmatrix} -F^h_{t-\Delta t} \\ -F^\theta_{t-\Delta t} \end{pmatrix} = \begin{pmatrix} p_h \sum_{j=1}^{Nl} \beta_{j+1} h_{t-j\Delta t} \\ p_\theta \sum_{j=1}^{Nl} \beta_{j+1} \theta_{t-j\Delta t} \end{pmatrix} \tag{14}$$

where: $p_h = \frac{l_x l_y}{l_z}$ and $p_\theta = \frac{\Theta}{4}\frac{({R_e}^4 - {R_i}^4)}{l_x}$ depend on the geometry of the viscoelastic dampers.

Incorporating the viscoelastic damping in the equation of motion, Eq. (7), results in:

$$\bar{\boldsymbol{M}}\ddot{\mathbf{q}} + \bar{\boldsymbol{C}}\dot{\mathbf{q}} + \bar{\boldsymbol{K}}_{\boldsymbol{v}}^{\boldsymbol{nl}}\mathbf{q} = \mathbf{F_v} \tag{15}$$

where the matrices $\bar{\boldsymbol{M}}$ and $\bar{\boldsymbol{C}}$ are, respectively, the complete mass and damping matrices with the augmented aerodynamic lag states and piezoelectric feature, previously described in Eq. (7):

$$\bar{\boldsymbol{M}} = \begin{pmatrix} \tilde{\boldsymbol{M}} & \mathbf{0} & \mathbf{0} \\ -\boldsymbol{b}_1 & \mathbf{0} & \mathbf{0} \\ \mathbf{0} & \mathbf{0} & 0 \end{pmatrix} \tag{16}$$

$$\bar{\boldsymbol{C}} = \begin{pmatrix} \tilde{\boldsymbol{C}} & \mathbf{0} & \mathbf{0} \\ -\boldsymbol{b}_2 & \boldsymbol{I} & \mathbf{0} \\ \mathbf{H} & \mathbf{0} & C_{eq} \end{pmatrix} \tag{17}$$

Similarly, $\bar{\boldsymbol{K}}_{\boldsymbol{v}}^{\boldsymbol{nl}}$ is the complete stiffness matrix, which incorporates the nonlinear and viscoelastic stiffness terms, the lag states, and the

piezoelectric effect:

$$\bar{\boldsymbol{K}}_{\boldsymbol{v}}^{\boldsymbol{nl}} = \begin{pmatrix} \bar{\boldsymbol{K}}_{\boldsymbol{v}}^{\boldsymbol{nl}} & -\boldsymbol{a}_4 & \mathbf{H}^{\mathrm{T}} \\ -\boldsymbol{b}_3 & -\boldsymbol{b}_4 & \mathbf{0} \\ \mathbf{0} & \mathbf{0} & R^{-1} \end{pmatrix} \tag{18}$$

where $\bar{\boldsymbol{K}}_{\boldsymbol{v}}^{\boldsymbol{nl}} = \begin{pmatrix} {k_h}^{nl} & 0 \\ 0 & {k_\theta}^{nl} \end{pmatrix} + \begin{pmatrix} k_{h,fp}^{v} & 0 \\ 0 & {k_\theta}^{v} \end{pmatrix} - \boldsymbol{a}_3$ represents the new stiffness matrix with the combined effects of the structural nonlinearities and the viscoelastic stiffness. Lastly, $\mathbf{F_v}$ represents the dissipative forces introduced by the viscoelastic dampers: $\mathbf{F_v} = \begin{pmatrix} -F_{t-\Delta t}^{h} & -F_{t-\Delta t}^{\theta} & 0 & 0 & 0 \end{pmatrix}^{\mathrm{T}}$.

The flutter speed of the linear airfoil without viscoelastic damping, termed baseline airfoil, can be obtained from the eigenvalues λ of the system state matrix $\boldsymbol{A}$. As these are in the form $\lambda = -\zeta\omega \pm i\omega\sqrt{1-\zeta^2}$ [7], the system will display unstable behavior if the damping factor ζ becomes negative. The flutter condition is the neutral stability state in which there is no damping. Hence, the flutter speed is found by computing the eigenvalues of $\boldsymbol{A}$ for a set of flow speeds and identifying the speed that nullifies ζ of a given vibration mode. The relationship between the eigenvalue and the damping factor is $\zeta = -Re(\lambda)\left(Re(\lambda)^2 + Im(\lambda)^2\right)^{(-1/2)}$. The matrix $\boldsymbol{A}$ is detailed in Appendix B.

Numerical integration of Eq. (15) is used to obtain the response of the system. Following the Newmark method, the acceleration and speed vectors at the next instant of time are given, respectively, as:

$$\ddot{\mathbf{q}}_{t+\Delta t}^{k} = \frac{1}{\nu\Delta t^2}\left(\mathbf{q}_{t+\Delta t}^{k} - \mathbf{q}_t\right) - \frac{1}{\nu\Delta t}\dot{\mathbf{q}}_t - \left(\frac{1}{2\nu} - 1\right)\ddot{\mathbf{q}}_t \tag{19}$$

and

$$\dot{\mathbf{q}}_{t+\Delta t}^{k} = \dot{\mathbf{q}}_t + \Delta t\,(1-\delta)\,\ddot{\mathbf{q}}_t + \delta\Delta t\ddot{\mathbf{q}}_{t+\Delta t}^{k} \tag{20}$$

which are substituted in Eq. (15) to define the residue $\mathbf{R}_{t+\Delta t}^{k-1}$:

$$\mathbf{R}_{t+\Delta t}^{k-1} = \left(\bar{\boldsymbol{K}}_{\boldsymbol{v}}^{\boldsymbol{nl}} + \boldsymbol{\Xi}_{t+\Delta t}^{1}\right)\mathbf{q}_{t+\Delta t}^{k-1} - \boldsymbol{\Xi}_{t+\Delta t}^{1}\mathbf{q}_t - \boldsymbol{\Xi}_{t+\Delta t}^{2}\dot{\mathbf{q}}_t - \boldsymbol{\Xi}_{t+\Delta t}^{3}\ddot{\mathbf{q}}_t - \mathbf{F_v} \tag{21}$$

where:

$$\boldsymbol{\Xi}_{t+\Delta t}^{1} = \frac{1}{\nu\Delta t^2}\bar{\boldsymbol{M}} + \frac{\delta}{\nu\Delta t}\bar{\boldsymbol{C}} \tag{22}$$

$$\boldsymbol{\Xi}_{t+\Delta t}^{2} = \frac{1}{\nu\Delta t}\bar{\boldsymbol{M}} + \left(\frac{\delta}{\nu} - 1\right)\bar{\boldsymbol{C}} \tag{23}$$

Table 2 Parameters of the two dof energy harvesting airfoil [8,39]

Parameter	Value	Parameter	Value
b	0.145 m	c_h	1.2113 Ns/m
l	0.8 m	c_θ	0.0043 Ns
a	–0.1379	ω_h	14.954 rad/s
x_θ	0.1897	ω_θ	26.955 rad/s
r_θ	0.064 m	α	1.55 mN/V
ρ	1.119 kg/m^3	C_{eq}	120 nF
$\bar{m}$	13.5 kg	R	100 kΩ
m	6.5 kg		

$$\Xi^3_{t+\Delta t} = \left(\frac{1}{2\nu} - 1\right)\bar{\boldsymbol{M}} + \frac{\Delta t}{2}\left(\frac{\delta}{\nu} - 2\right)\bar{\boldsymbol{C}} \tag{24}$$

The residue is to be minimized by iterative computation of $\mathbf{q}^k_{t+\Delta t}$ through the Newton-Raphson method. Hence, k represents a given iteration. By assuming constant acceleration, the Newmark's parameters are $\nu = 1/4$ and $\delta = 1/2$. These values make the Newmark method unconditionally stable [38].

3 Nonlinear parametric study of the piezoaeroelastic airfoil

This section evaluates the effect of nonlinear springs with hardening and free-play to determine a favorable condition for energy harvesting. So far, there has been no viscoelastic damping. The airfoil considered is a NACA 0012 profile, which was studied by [39] without the harvesting circuit. Its parameters are in Table 2. Since the flap does not move, the airfoil only has the pitch and plunge dofs. The specifications of the energy harvesting circuit are also in Table 2, based on the usual values found in the literature for similar flutter energy harvesting systems [8,18].

For the baseline airfoil without the energy harvesting circuit and with linear springs ($a^h_0 = 1$, $a^h_1 = 0$, $a^\theta_0 = 1$, $a^\theta_1 = 0$), flutter happens at $V^* = 14.01$ m/s (Fig. 3), agreeing with the experimental measures of [39], who found the flutter speed to be around 14 m/s. The results will display the flow speed V normalized by the critical speed of the linear airfoil, V^*, where $\bar{V} = V/V^*$, to simplify the distinction between the subcritical and supercritical regions.

3.1 Hardening effect on the nonlinear pitch and plunge springs. Initially, there is no free-play ($h_{fp} = 0$, $\theta_{fp} = 0$) and only cubic non-linearity in stiffness. The nonlinear coefficients are varied from the following reference configuration: $a^h_0 = 1$, $a^h_1 = 1$, $a^\theta_0 = 1$, $a^\theta_1 = 10$ to evaluate the influence of the nonlinear springs on each degree of freedom. Figure 4(*a*) and Fig. 4(*b*) show the reduction in amplitude of h and θ with increasing hardening coefficient in pitch (a^θ_1). This hardening effect benefits energy harvesting as it may be employed to control the vibration amplitude in the post-flutter regime, thus allowing safe operation for a wider flow speed range before oscillations reach a prohibitive amplitude. The reduction in amplitude due to the increase in the nonlinear coefficient imposes a reduction in the voltage and power produced at a given flow speed, as illustrated by Fig. 4(*c*) and Fig. 4(*d*). Thus, there is a compromise between harvested power and operational speed range for hardening in pitch, whereas the effect of hardening in plunge (a^h_1) is negligible, as illustrated by Fig. 5(*a*). Furthermore, because of the electromechanical coupling in the plunge dof, the voltage behavior concerning the flow speed is similar to that of the plunge dof.

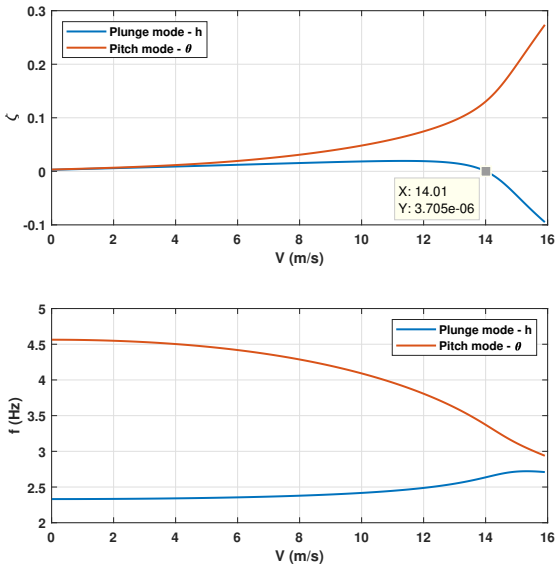

Fig. 3 Damping factor and natural frequencies versus the flow speed for each vibration mode.

3.2 Free-play effect on the nonlinear pitch and plunge springs. From Fig. 4 and Fig. 5, it is clear that the cubic non-linearity creates a supercritical Hopf bifurcation, implying there is no energy harvesting before the critical flutter speed. However, free-play addition in the hardening springs may generate LCOs prematurely, in a subcritical fashion, thus allowing power generation at lower speeds. Therefore, their introduction in the nonlinear springs is considered. The same reference configuration for the stiffness coefficients is kept: $a_0^h = 1$, $a_1^h = 1$, $a_0^\theta = 1$, $a_1^\theta = 10$.

Adding free-play to the nonlinear plunge spring alone does not produce any response for the flow speed range considered (Fig. 5(*b*)). If there is free-play in the nonlinear pitch spring, one obtains a more interesting result.. For this configuration, an increasing amount of θ_{fp} results in a higher amplitude at a given flow speed (Fig. 6(*a*)). This behavior is desirable for energy harvesting, as the increased amplitude results in higher power (Fig. 6(*b*)) compared with the case without free-play. For instance, at $\bar{V} = 1$, an over 2000 % gain is observed for $\theta_{fp} = 2°$. Moreover, the Hopf bifurcation becomes subcritical, meaning harvesting can start before the linear flutter speed. Within this regard, the increment of the free-play gap reduces the flutter onset until a certain point, after which there is an opposite trend, suggesting the existence of an optimal free-play gap for pitch. The maximum reduction observed is about 3 %.

Another implication of the subcritical regime is that different bifurcation points may be obtained depending on whether the numerical integration is made by increasing or decreasing the flow speed, as displayed in Fig. 7(*a*) for $\theta_{fp} = 1°$. Thus, the minimum speed that may achieve harvesting can be further reduced, up to 37 %. The bifurcation occurs at a lower speed when the flow speed is swept downward. By adding free-play to the nonlinear plunge spring, premature bifurcation can also happen when sweeping the speed upward (Fig. 7(*b*)). Even the amount of $h_{fp} = 0.5$ mm is enough to make both paths almost match. This behavior is desirable for harvesting, as the operational speed range extends regardless of whether the flow speed increases or decreases. It is worth mentioning that unless otherwise stated, all results are for an increasing flow speed.

The coefficient h_{fp} is incremented in Fig. 8(*a*) to further investigate its impact on the system performance. The influence of h_{fp} is mainly in the subcritical regime, where it reduces the onset of bifurcation. Regardless of the amount of h_{fp}, all amplitudes converge to

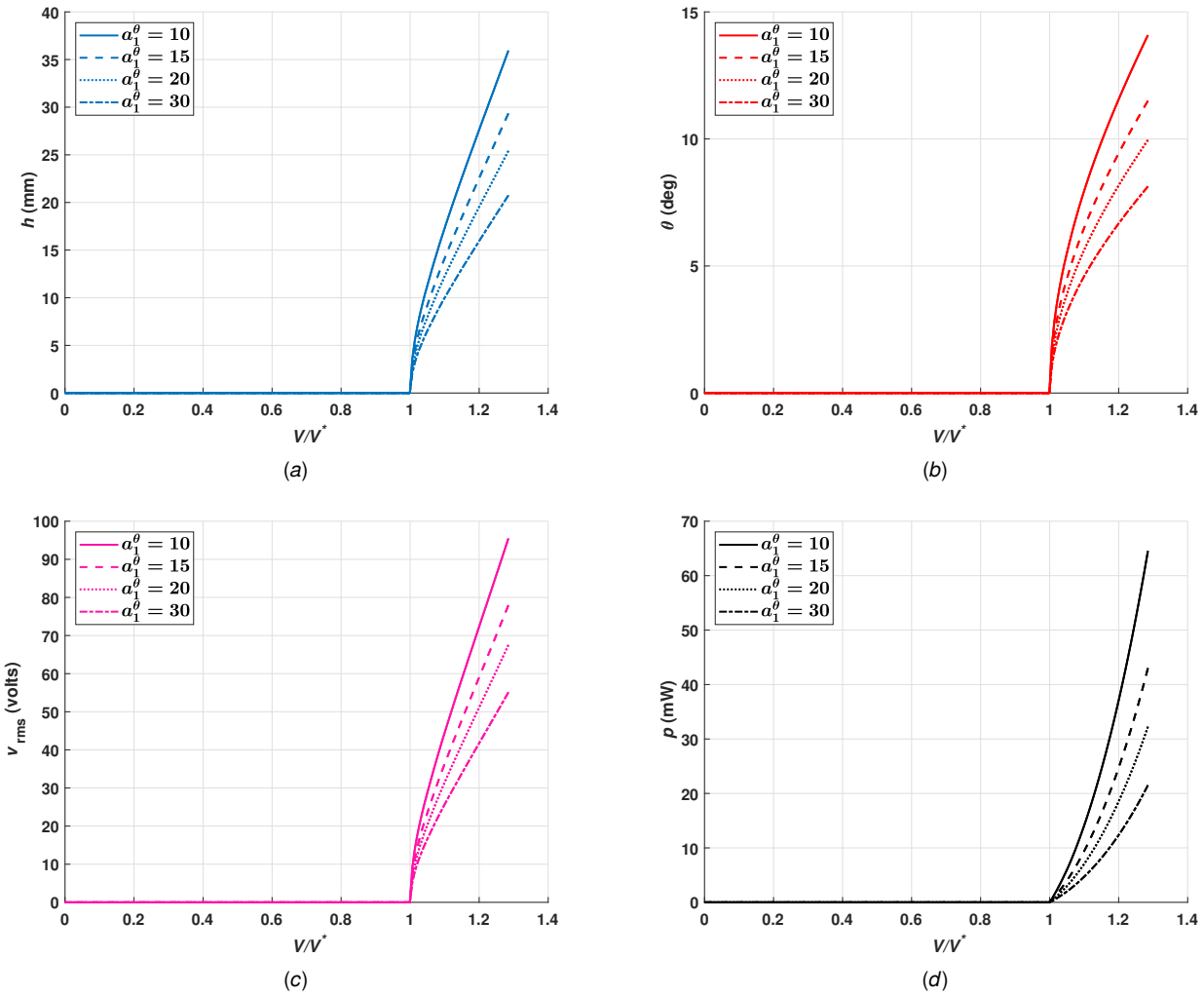

Fig. 4 Sensitivity of plunge (*a*), pitch (*b*), voltage (*c*) and power (*d*) bifurcation diagrams to the hardening coefficient a_1^θ for the case without free-play in the nonlinear springs.

the same curve as the flow speed increases.

4 Combination of viscoelastic damping with structural nonlinearities

After establishing the effects of hardening and free-play nonlinearities, this study examines the effect of viscoelastic damping from an energy-harvesting perspective. One should mention that the term "viscoelastic damping" implies the addition of damping itself from the dissipative forces $\mathbf{F_v}$ (Eq. (15)) and stiffness (Eq. (18)). At first, it might seem counterintuitive that damping and stiffness could improve harvesting. However, for a discontinuous nonlinear system, it is not possible to determine beforehand how the stiffness and dissipative properties of each mode will influence the system at a particular airspeed after the onset of flutter, particularity considering the modal coupling characteristic of this phenomenon (Fig. 3). As the damping of a vibration mode becomes negative in the post-flutter regime, the increase of damping could increase the vibration amplitude and, by extension, the harvested power, as demonstrated in Ref. [31]. Furthermore, the relationship between stiffness and power is another example of non-monotonic behavior [15,16,30]. Therefore, the stiffness and dissipative forces of the viscoelastic damper could favor energy harvesting, motivating the parametric study proposed.

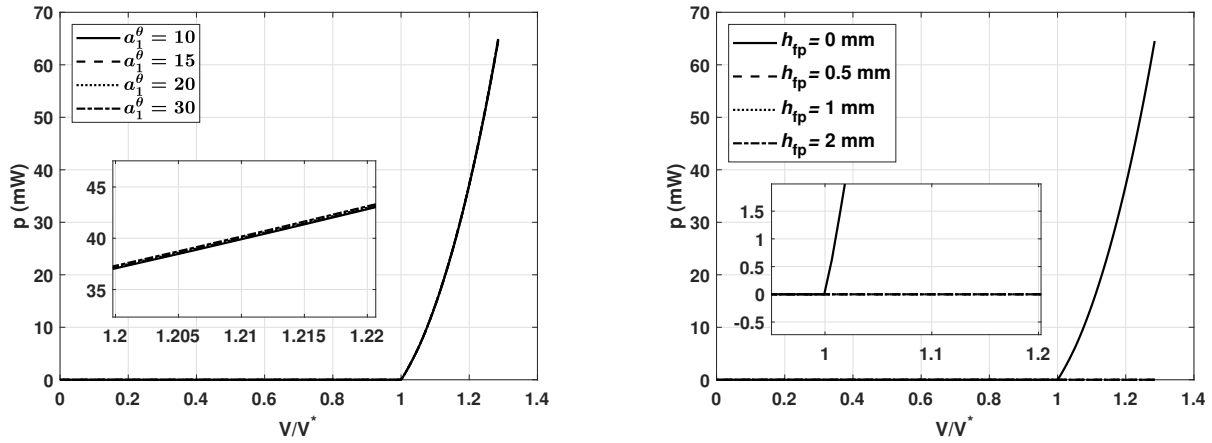

(*a*) (*b*)

Fig. 5 Sensitivity of power bifurcation diagram to the hardening coefficient a_1^h (*a*), and to the free-play in the plunge nonlinear spring h_{fp} (*b*).

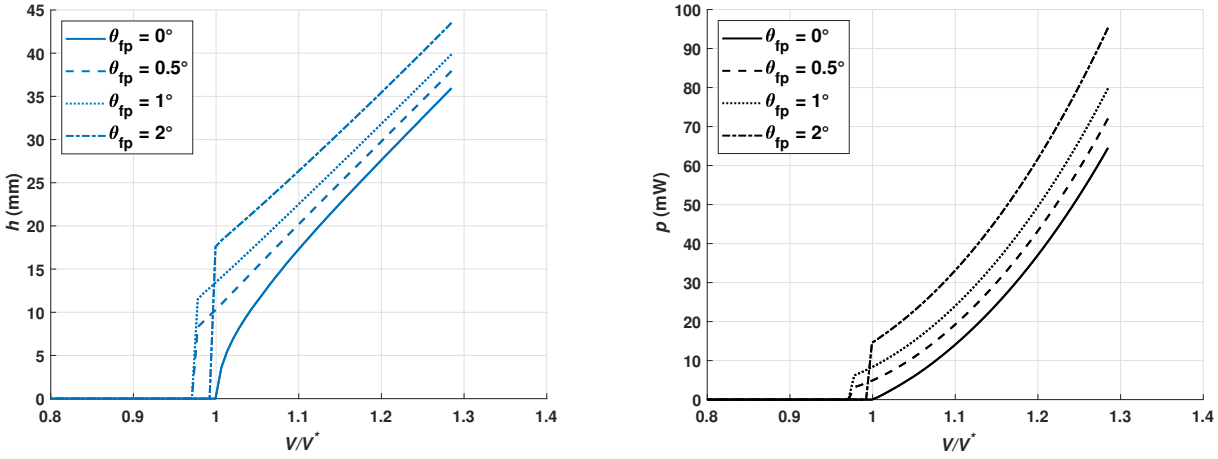

(*a*) (*b*)

Fig. 6 Sensitivity of plunge (*a*) and power (*b*) bifurcation diagrams to free-play in the pitch nonlinear spring (θ_{fp}).

4.1 Viscoelastic damping in pitch. Although the free-play in the nonlinear pitch and plunge springs favors energy harvesting, as previously discussed, it may lead to complex phenomena such as chaos [40]. Viscoelastic damping can be added in the pitch dof to prevent this undesirable behavior, following the configuration of Fig. 2. For the free-play combination h_{fp} = 2 mm and θ_{fp} = 1° in Fig. 8(*b*), it is possible to stabilize the response by adding only a small amount of viscoelastic material. Moreover, adding viscoelastic damping can further anticipate the onset of flutter by about 13 %. The opposite trend happens as the thickness increases, and there is a delay in the bifurcation. This behavior comes with improved power at supercritical speeds. The effect of viscoelastic damping on the voltage response is in Fig. 9. The limit cycle becomes less complex and periodic as due to viscoelastic damping.

Again, it is necessary to note that by imposing a given maximum allowable vibration amplitude, there is a compromise between harvested power and operational speed range such that having overall higher power implies a shorter speed range and vice-versa, similar to the hardening effect discussed. In terms of harvested power, there is a tendency for the viscoelastic damping in pitch to yield higher power for most of the flow speed range compared to the configuration without it (Fig. 8(*b*)).

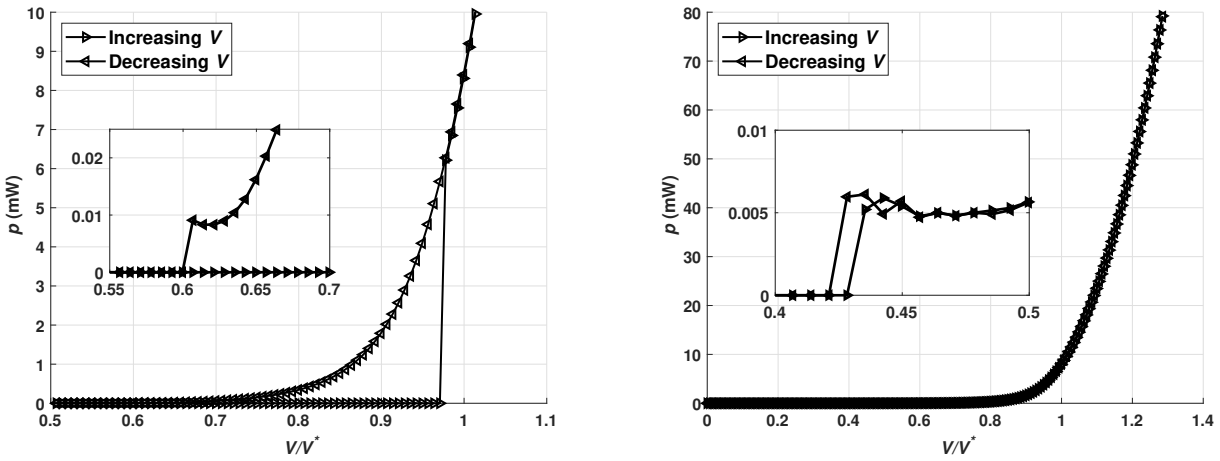

(*a*) (*b*)

Fig. 7 Power bifurcation diagrams when increasing and decreasing the flow speed for θ_{fp} = 1°, h_{fp} = 0 mm (*a*) and for θ_{fp} = 1°, h_{fp} = 0.5 mm (*b*).

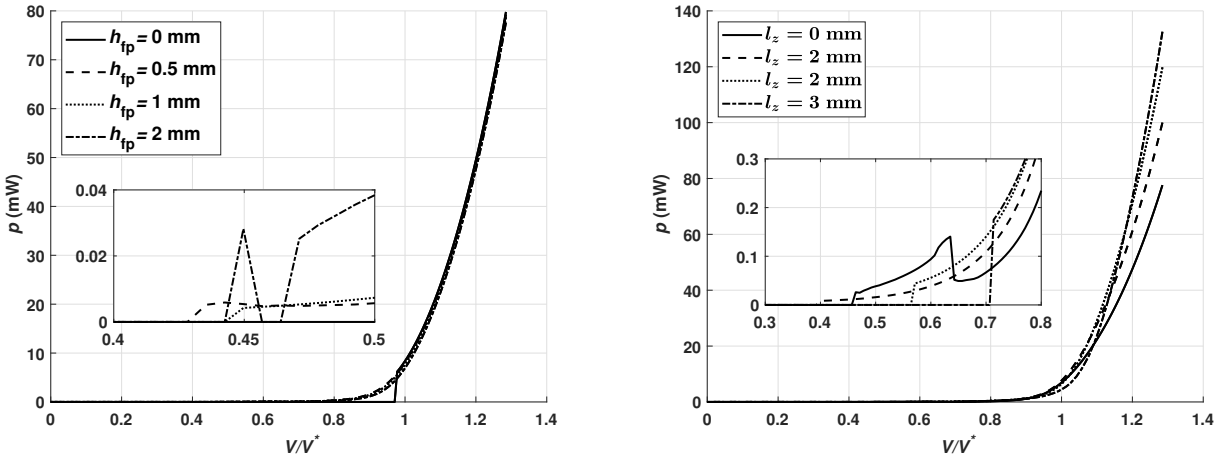

(*a*) (*b*)

Fig. 8 Sensitivity of power bifurcation diagrams to h_{fp} for θ_{fp} = 1° (*a*) and to the thickness of the viscoelastic damper (l_z) in pitch for θ_{fp} = 1°, h_{fp} = 2 mm and $\Theta = \pi$ (*b*).

So far, the temperature has been kept constant at 20°C. However, temperature dependence is a fundamental characteristic of viscoelastic materials. The temperature is changed to check whether the behavior in Fig. 8(*b*) holds. As in Fig. 10(*a*), there is a discontinuity for the temperature of 35°C due to the associated stiffness reduction of the viscoelastic material. In addition, increasing temperature causes an early onset of flutter due to loss of stiffness while harvested power decreases. One can avoid discontinuous bifurcations due to temperature change if a thicker viscoelastic damper is employed, as illustrated in Fig. 10(*b*) , although this comes at the cost of increasing the flow speed for harvesting. Nevertheless, the bifurcation is still subcritical. Furthermore, the overall temperature effect on the system is the same as in Fig. 10(*a*), meaning the higher the temperature, the earlier the flutter onset and the lower the harvested power. Thus, the benefits of viscoelastic damping in the pitch are evident, as it can prevent the occurrence of complex unwanted dynamical behavior, reduce the flow speed for energy harvesting, and increase the power in the supercritical regime.

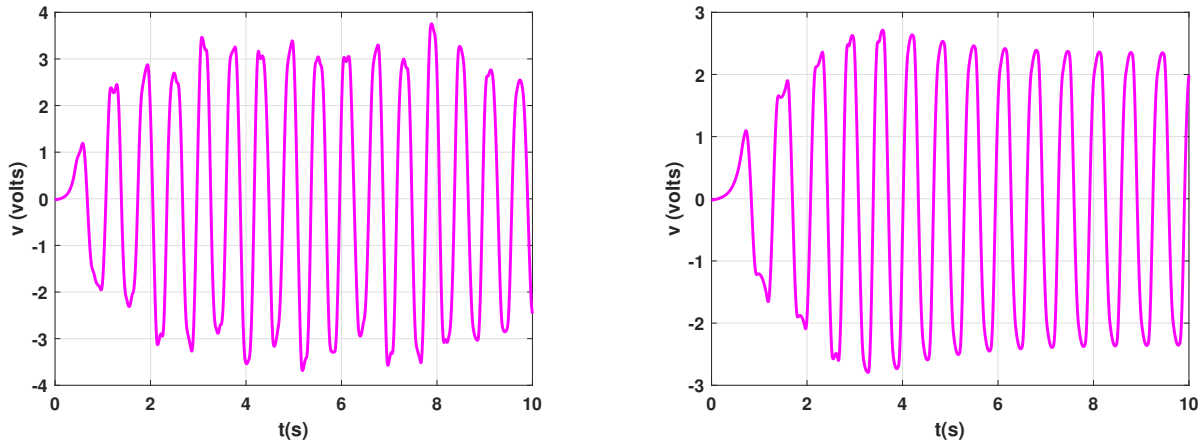

Fig. 9 Voltage time responses at $\bar{V}$ = 0.6 for h_{fp} = 2 mm, θ_{fp} = 1°, for the case without viscoelastic damping (l_z = 0 mm) (*a*) and with viscoelastic damper in pitch ($\Theta = \pi$, l_z = 1 mm) (*b*).

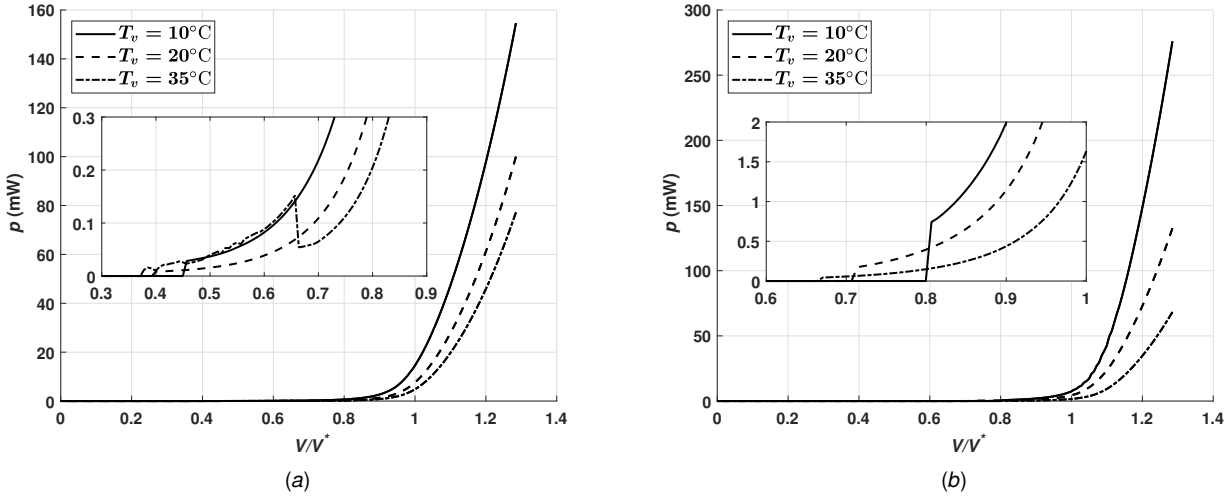

Fig. 10 Sensitivity of power bifurcation diagrams to temperature for the case study with free-play in the pitch and plunge nonlinear springs (θ_{fp} = 1°, h_{fp} = 2 mm) and viscoelastic damping in pitch ($\Theta = \pi$), where l_z = 1 mm (*a*) and l_z = 3 mm (*b*).

4.2 Viscoelastic damping in pitch and plunge. In all former cases, the focus was on the onset of the bifurcation and how a subcritical bifurcation could occur prematurely, as these are key aspects of flutter energy harvesting. Nonetheless, it is necessary to consider the need to control the vibration amplitude in the post-flutter, as excessive oscillations may damage the system or result in stall. Therefore, this paper evaluates the use of viscoelastic damping in the plunge dof to control the vibration amplitude at supercritical speeds. As there is no intention of losing the subcritical Hopf bifurcation obtained from combining the nonlinear springs with the viscoelastic damping in pitch, the idea is to add free-play to the viscoelastic material in plunge as illustrated by Fig. (2). Otherwise, the extra stiffness and damping could result in supercritical bifurcations, which are detrimental to the harvester's performance. The viscoelastic damping in plunge consists of two layers, defined by p_h = 24 mm. Figure 11 displays the effect of varying h^v_{fp} on the pitch, plunge, voltage, and power bifurcation diagrams. Initially, there is no difference among the curves. This behavior changes when the the system reaches the threshold h^v_{fp}, where it begins interacting with the viscoelastic component in plunge. The discontinuity in stiffness originates a

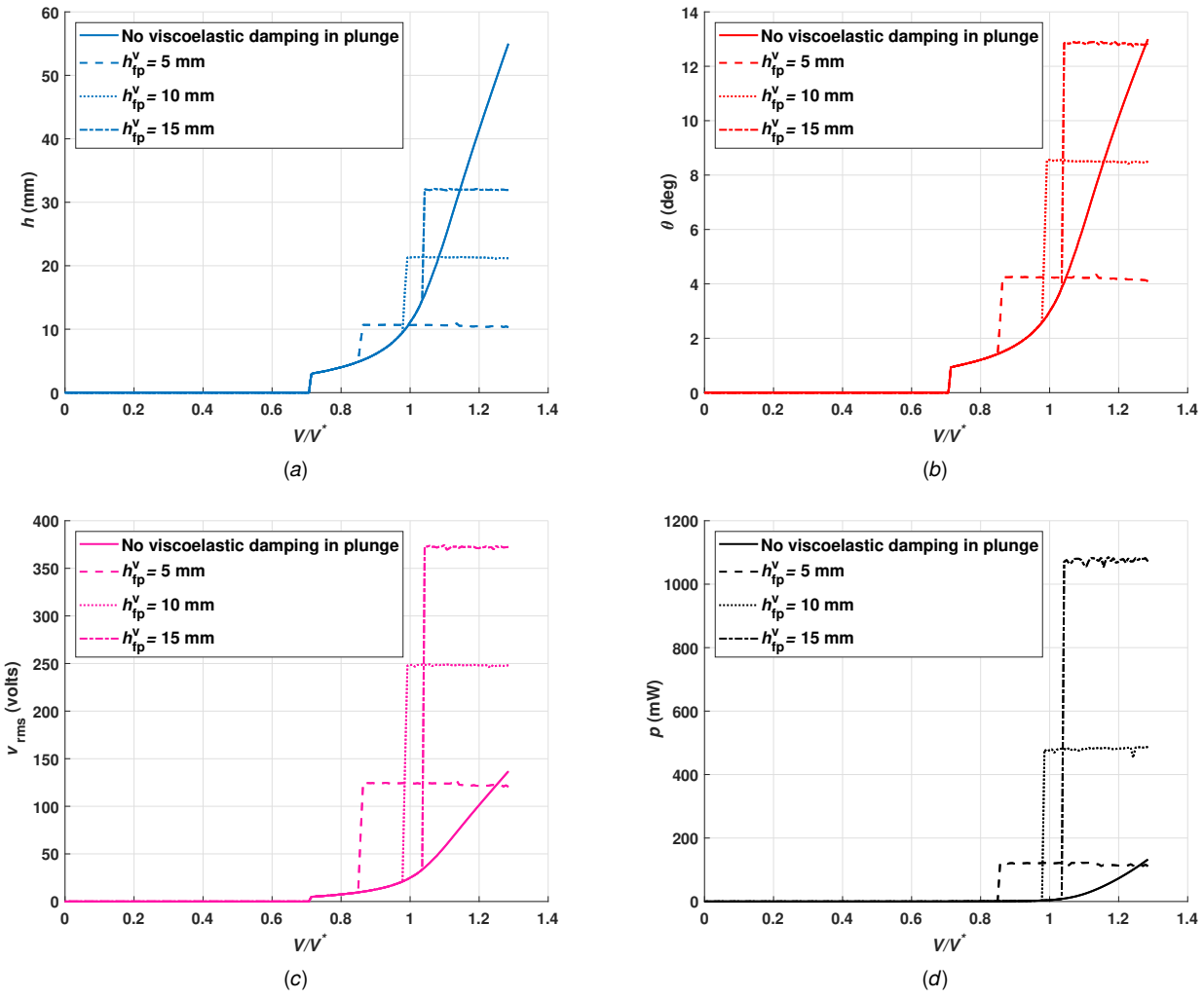

Fig. 11 Sensitivity of plunge (*a*), pitch (*b*), voltage (*c*) and power (*d*) bifurcation diagrams to h_{fp}^v for the case with free-play in the pitch and plunge nonlinear springs (θ_{fp} = 1°, h_{fp} = 2 mm), viscoelastic damping in pitch ($\Theta = \pi$, l_z = 3 mm) and in plunge (p_h = 24 mm).

sudden increase in vibration amplitude and thus in voltage and power, meaning that as h_{fp}^v decreases, a higher harvesting performance is achieved sooner compared to the case without viscoelastic damping in plunge. Moreover, the vibration amplitude has been contained and does not increase any longer with the airspeed, extending the operational speed range of the harvester. For instance, if a maximum vibration amplitude of 11 mm in plunge is selected, the configuration h_{fp}^v = 5 mm will make energy harvesting attainable between $0.86 \leq \bar{V} \leq 1.28$ in contrast to the $0.86 \leq \bar{V} \leq 0.99$ range of the case without viscoelastic damping, a 28 % gain. At $\bar{V} = 0.86$, the use of viscoelastic damping for h_{fp}^v = 5 mm represents a two-order power increase compared to the case without viscoelastic damping, which would reach that same amount of power only at $\bar{V} = 1.26$. By increasing h_{fp}^v, the system is allowed a higher amplitude, generating more power, but the sudden increase in voltage and power will occur at superior speeds. There is a compromise between the operational harvesting speed range and the power harvested in that range. The plunge and voltage time responses at $\bar{V} = 1.2$ are shown in Fig. 12. When the plunge amplitude reaches the value of h_{fp}^v = 10 mm around 2.5 s, the added stiffness of the viscoelastic damping increases the frequency of the LCO and its amplitude.

As stated previously, it is fundamental to quantify the effect of temperature on the performance of the proposed harvester. For the

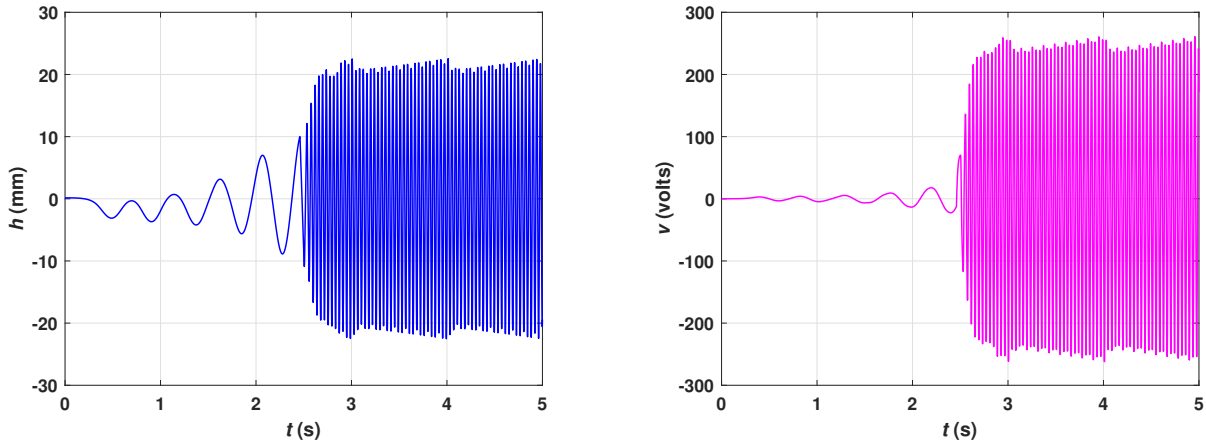

Fig. 12 Plunge (*a*) and voltage, (*b*) time responses at $\bar{V}$ = 1.2 for the case study with free-play in the pitch and plunge nonlinear springs (θ_{fp} = 1°, h_{fp} = 2 mm), viscoelastic damping in pitch ($\Theta = \pi$, t_v = 3 mm) and in plunge (p_h = 24 mm, h^v_{fp} = 10 mm).

case with h^v_{fp} = 10 mm, Fig. 13 shows that increasing the temperature lowers the cut-in speed due to the reduced stiffness. However, in the post-flutter regime, the higher temperature is not associated with the higher vibration amplitude. The lower temperature of T_v = 10°C causes the higher amplitude. Furthermore, increasing temperature is detrimental to the harvested power. The incorporation of the viscoelastic material with free-play in plunge does not change the subcritical Hopf bifurcation dynamic, favoring energy harvesting.

5 Conclusions

Motivated by the non-monotonic relationship between stiffness and damping in nonlinear aeroelastic systems, this work proposed the unprecedented combination of viscoelastic damping with hardening and free play nonlinearities to enhance the performance of a two-dof flutter energy harvesting system. The results indicate that the hardening spring in pitch has a superior influence on the system behavior than the one in plunge , and the cubic coefficient in pitch can tune the compromise between vibration amplitude and power at supercritical flow speeds. Regarding free-play, its addition to the nonlinear pitch spring can improve the voltage and power outputs of the harvester, the main benefit being a sudden increase at the onset of flutter. The power enhancement can exceed 2,000 %. Another advantage of incorporating free-play into the pitch hardening spring is the creation of a subcritical bifurcation, allowing energy harvesting at speeds inferior to the linear onset of flutter, with a reduction of 3 %. This effect improves with the introduction of free-play in the nonlinear plunge spring, extending the operational speed range to 37 %. However, increasing the free-play gap in the plunge nonlinear spring may lead to potentially unwanted complex dynamical behavior. The proposed viscoelastic damping in pitch can be employed to address this inconvenience, generating a periodic response. Also, it can further reduce the flow speed to achieve energy harvesting by 13 %. Moreover, the viscoelastic damping in the plunge dof can passively control the vibration amplitude for supercritical flow speeds, thus widening the operational flow speed range to obtain persistent power generation. There was a 28 % increase in the operational speed range. The additional stiffness provided by the viscoelastic damper enhanced the system's ability to store energy in the supercritical regime, resulting in a substantial power increase. Viscoelastic dampers conserve a favorable behavior for harvesting for the temperature range of 10°C to 35°C. Therefore, viscoelastic damping may represent a way to fine-tune the FEH system, highlighting the relevance of the parametric analysis proposed in this study. Future work will focus on the experimental validation of the numerical model.

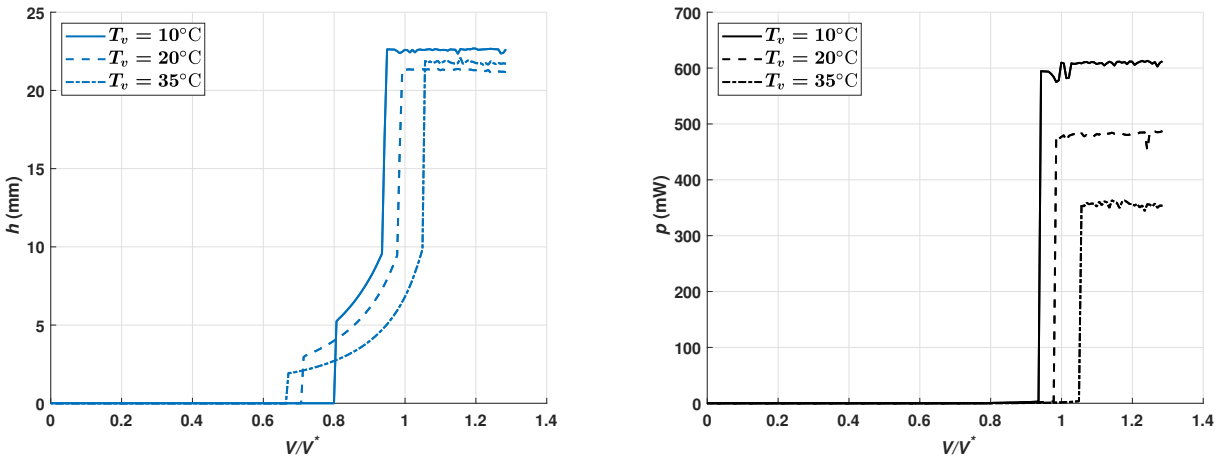

(*a*) (*b*)

Fig. 13 Sensitivity of plunge (*a*) and power (*b*) bifurcation diagrams to temperature for the case study with free-play in the pitch and plunge nonlinear springs (θ_{fp} = 1°, h_{fp} = 2 mm), viscoelastic damping in plunge (p_h = 24 mm, h^{γ}_{fp} = 10 mm) and in pitch ($\Theta = \pi$, l_z = 3 mm).

Acknowledgment

The authors thank CAPES, CNPq, and FAPEMIG for continued financial support for their research activities. It is also important to express acknowledgments to the Federal University of Uberlândia in Brazil and the FEMTO-ST Institute at Besançon, France, for the facilities provided.

Funding Data

- Coordenação de Aperfeiçoamento de Pessoal de Nível Superior, CAPES (APQ-01865 and 88887.846927/2023-00)
- Conselho Nacional de Desenvolvimento Científico e Tecnológico, CNPq (306138/2019-0)
- Fundação de Amparo à Pesquisa do Estado de Minas Gerais, FAPEMIG (PPM-0058-18)

Nomenclature

b = airfoil semi-chord (m)

C_{eq} = equivalent capacitance (F)

c = damping coefficient (N s m^{-1})

F = dissipative efforts (N)

G = low frequency shear modulus (Pa)

h = plunge degree of freedom (m)

I = moment of inertia (kg m^2)

k = stiffness coefficient (N m^{-1})

L = lift force per unit of span (N m^{-1})

l = airfoil span (m)

l_x = width of the viscoelastic damper (m)

l_y = length of the viscoelastic damper (m)

l_z = thickness of the viscoelastic damper (m)

M = pitching moment per unit of span (N)

m = airfoil mass (kg)

$\bar{m}$ = total mass (kg)

N_l = memory size (s)

p_h = geometric factor of the viscoelastic damper in plunge (m)

p_θ = geometric factor of the viscoelastic damper in pitch (m^3)

Q = downwash at 3/4 of the chord (m s^-1)

R = electrical resistance (Ω)

R_e = external radius of the viscoelastic damper in pitch (m)

R_i = internal radius of the viscoelastic damper in pitch (m)

r_θ = radius of gyration (m)

t = time (s)

U = strain energy (J)

V = airspeed (m s^{-1})

$\tilde{V}$ = volume (m^3)

v = voltage (V)

Greek Letters

α = electromechanical coupling term (N V^{-1})

β_{j+1} = recurrent term of the fractional derivative method (Pa)

γ_1 = curve fitting coefficient of the fractional derivative representation (Pa s)

γ_2 = curve fitting coefficient of the fractional derivative representation (s)

Δt = time step (s)

Θ = angular perimeter of the viscoelastic damper in pitch (rad)

λ = state matrix eigenvalue (rad s^{-1})

ρ = air density (kg m^{-3})

τ_t = shear stress at a given time instant (Pa)

$\chi_{1,2}$ = aerodynamic lag states (m $^{-1}$)

ω = undamped natural frequency (s^{-1})

Dimensionless Groups

A_j = Grünwald coefficients

a = location of the elastic axis

$a_0^{h,\theta}$ = linear stiffness coefficient

$a_1^{h,\theta}$ = cubic stiffness coefficient

N = number of points used to set the memory size

$\bar{V}$ = normalized airspeed

x_θ = offset between the elastic axis and the center of gravity

δ = Newmark velocity parameter

ϵ_t = strain at a given time instant

θ = pitch degree of freedom

ξ = fractional order of the time derivative

ν = Newmark acceleration parameter

ζ = damping factor

Superscripts and Subscripts

fp = free play

h = associated with the plunge dof

l = linear term

nl = nonlinear term

θ = associated with the pitch dof

$*$ = at the linear flutter condition

Appendix A: Aerodynamic matrices

The aerodynamic matrices $\boldsymbol{a}_j$ and $\boldsymbol{b}_j$ obtained from the Jones approximation to the Wagner function are given by the following equations:

$$\boldsymbol{a}_1 = l\begin{pmatrix} -\pi b^2\rho & \pi b^3\rho a \\ \pi b^3\rho a & -\pi b^{-4}\rho\left(\frac{1}{8}+a^2\right) \end{pmatrix} \tag{A1}$$

$$\begin{aligned} \boldsymbol{a}_2 = l\begin{pmatrix} -2\pi\rho V b & 0 \\ 2b^2\left(a+\frac{1}{2}\right)\pi\rho V & 0 \end{pmatrix} \\ +l\begin{pmatrix} 0 & -2\pi\rho V b^2\,(1-a) \\ 0 & \left[-\pi b^3\rho + 2b^3\left(a+\frac{1}{2}\right)\pi\rho\right] V\left(\frac{1}{2}-a\right) \end{pmatrix} \end{aligned} \tag{A2}$$

$$\boldsymbol{a}_3 = l\begin{pmatrix} 0 & -2\pi\rho V^2 b \\ 0 & 2b^2\left(a+\frac{1}{2}\right)\pi\rho V^2 \end{pmatrix} \tag{A3}$$

$$\boldsymbol{a}_4 = l\begin{pmatrix} -2\pi\rho V b & -2\pi\rho V b \\ 2b^2\left(a+\frac{1}{2}\right)\pi\rho V & 2b^2\left(a+\frac{1}{2}\right)\pi\rho V \end{pmatrix} \tag{A4}$$

$$\boldsymbol{b}_1 = \begin{pmatrix} -0.165 & -0.165b\,(0.5-a) \\ -0.335 & -0.335b\,(0.5-a) \end{pmatrix} \tag{A5}$$

$$\boldsymbol{b}_2 = \begin{pmatrix} 0 & -0.165V \\ 0 & -0.335V \end{pmatrix} \tag{A6}$$

$$\boldsymbol{b}_3 = \begin{pmatrix} 0 & 0 \\ 0 & 0 \end{pmatrix} \tag{A7}$$

$$\boldsymbol{b}_4 = \begin{pmatrix} -0.041\frac{V}{b} & 0 \\ 0 & -0.320\frac{V}{b} \end{pmatrix} \tag{A8}$$

Appendix B: System State Matrix

By imposing linear springs in Eq. (7), $a_0^h = a_0^\theta = 1$, $a_1^h = a_1^\theta = 0$, the state space representation is $\dot{\mathbf{y}} = \boldsymbol{A}\mathbf{y}$, where $\mathbf{y} = \begin{pmatrix} h & \theta & \dot{h} & \dot{\theta} & \chi_1 & \chi_2 & v \end{pmatrix}^{\mathrm{T}}$ and the matrix $\boldsymbol{A}$ is given by:

$$\boldsymbol{A} = \begin{pmatrix} \mathbf{0} & \boldsymbol{I} & \mathbf{0} & \mathbf{0} \\ \boldsymbol{A}_{21} & \boldsymbol{A}_{22} & \boldsymbol{A}_{23} & \mathbf{A}_{24} \\ \boldsymbol{A}_{31} & \boldsymbol{A}_{32} & \boldsymbol{A}_{33} & \mathbf{A}_{34} \\ \mathbf{0} & \mathbf{A}_{42} & \mathbf{0} & A_{44} \end{pmatrix} \tag{B1}$$

where:

$$\boldsymbol{A}_{21} = -\tilde{\boldsymbol{M}}^{-1}\tilde{\boldsymbol{K}} \tag{B2}$$

$$\boldsymbol{A}_{22} = -\tilde{\boldsymbol{M}}^{-1}\tilde{\boldsymbol{C}} \tag{B3}$$

$$\boldsymbol{A}_{23} = \tilde{\boldsymbol{M}}^{-1}\boldsymbol{a}_4 \tag{B4}$$

$$\mathbf{A}_{24} = \tilde{\boldsymbol{M}}^{-1}\mathbf{H}^{\mathrm{T}} \tag{B5}$$

$$\boldsymbol{A}_{31} = \boldsymbol{b}_3 - \boldsymbol{b}_1\left(\tilde{\boldsymbol{M}}^{-1}\tilde{\boldsymbol{K}}\right) \tag{B6}$$

$$\boldsymbol{A}_{32} = \boldsymbol{b}_2 - \boldsymbol{b}_1\left(\tilde{\boldsymbol{M}}^{-1}\tilde{\boldsymbol{C}}\right) \tag{B7}$$

$$\boldsymbol{A}_{33} = \boldsymbol{b}_4 - \boldsymbol{b}_1\left(\tilde{\boldsymbol{M}}^{-1}\boldsymbol{a}_4\right) \tag{B8}$$

$$\mathbf{A}_{34} = \boldsymbol{b}_1\tilde{\boldsymbol{M}}^{-1}\mathbf{H}^{\mathrm{T}} \tag{B9}$$

$$\mathbf{A}_{42} = -{C_{eq}}^{-1}\mathbf{H} \tag{B10}$$

$$A_{44} = -\left(RC_{eq}\right)^{-1} \tag{B11}$$

References

[1] Zhou, W., Du, D., Cui, Q., Lu, C., Wang, Y., and He, Q., 2022, "Recent Research Progress in Piezoelectric Vibration Energy Harvesting Technology," Energies, **15**(3), p. 947.

[2] Li, Z., Zhou, S., and Yang, Z., 2022, "Recent progress on flutter-based wind energy harvesting," International Journal of Mechanical System Dynamics, **2**(1), pp. 82–98.

[3] Abdelkefi, A., 2016, "Aeroelastic energy harvesting: A review," International Journal of Engineering Science, **100**, pp. 112–135.

[4] Bonnin, M., Traversa, F. L., and Bonani, F., 2021, "Leveraging circuit theory and nonlinear dynamics for the efficiency improvement of energy harvesting," Nonlinear Dynamics, **104**(1), pp. 367–382.

[5] Liu, S., Li, P., and Yang, Y., 2018, "On the design of an electromagnetic aeroelastic energy harvester from nonlinear flutter," Meccanica, **53**(11-12), pp. 2807–2831.

[6] Li, Z., Zhou, S., and Li, X., 2022, "A piezoelectric–electromagnetic hybrid flutter-based wind energy harvester: Modeling and nonlinear analysis," International Journal of Non-Linear Mechanics, **144**, p. 104051.

[7] Wright, J. R. and Cooper, J. E., 2015, *Introduction to Aircraft Aeroelasticity and Loads* , 2nd ed., Wiley.

[8] Erturk, A., Vieira, W. G. R., De Marqui, C., and Inman, D. J., 2010, "On the energy harvesting potential of piezoaeroelastic systems," Applied Physics Letters, **96**(18), p. 184103.

[9] Erturk, A. and Inman, D. J., 2011, *Piezoelectric Energy Harvesting*, Wiley.

[10] Lee, B., Price, S., and Wong, Y., 1999, "Nonlinear aeroelastic analysis of airfoils: bifurcation and chaos," Progress in Aerospace Sciences, **35**(3), pp. 205–334.

[11] Basta, E., Ghommem, M., and Emam, S., 2021, "Flutter control and mitigation of limit cycle oscillations in aircraft wings using distributed vibration absorbers," Nonlinear Dynamics, **106**(3), pp. 1975–2003.

[12] Bryant, M. and Garcia, E., 2009, "Development of an aeroelastic vibration power harvester," p. 728812, doi: 10.1117/12.815785.

[13] Bryant, M. and Garcia, E., 2009, "Energy harvesting: a key to wireless sensor nodes," p. 74931W, doi: 10.1117/12.845784.

[14] Bryant, M. and Garcia, E., 2011, "Modeling and Testing of a Novel Aeroelastic Flutter Energy Harvester," Journal of Vibration and Acoustics, **133**(1).

[15] Sousa, V. C., de M Anicézio, M., De Marqui Jr, C., and Erturk, A., 2011, "Enhanced aeroelastic energy harvesting by exploiting combined nonlinearities: theory and experiment," Smart Materials and Structures, **20**(9), p. 094007.

[16] Abdelkefi, A., Nayfeh, A. H., and Hajj, M. R., 2012, "Modeling and analysis of piezoaeroelastic energy harvesters," Nonlinear Dynamics, **67**(2), pp. 925–939.

[17] Wan, C., Tian, H., Shan, X., and Xie, T., 2023, "Enhanced performance of airfoil-based piezoelectric energy harvester under coupled flutter and vortex-induced vibration," International Journal of Mechanical Sciences, **241**, p. 107979.

[18] Bouma, A., Le, E., Vasconcellos, R., and Abdelkefi, A., 2022, "Effective design and characterization of flutter-based piezoelectric energy harvesters with discontinuous nonlinearities," Energy, **238**, p. 121662.

[19] Bouma, A., Vasconcellos, R., and Abdelkefi, A., 2023, "Nonlinear modeling, characterization, and effectiveness of three-degree-of-freedom piezoaeroelastic energy harvesters," Mechanical Systems and Signal Processing, **189**, p. 110103.

[20] Tian, W., Li, Y., Yang, Z., Li, P., and Zhao, T., 2020, "Suppression of nonlinear aeroelastic responses for a cantilevered trapezoidal plate in hypersonic airflow using an energy harvester enhanced nonlinear energy sink," International Journal of Mechanical Sciences, **172**, p. 105417.

[21] Cunha-Filho, A., de Lima, A., Donadon, M., and Leão, L., 2016, "Flutter suppression of plates using passive constrained viscoelastic layers," Mechanical Systems and Signal Processing, **79**, pp. 99–111.

[22] Cunha-Filho, A., de Lima, A., Donadon, M., and Leão, L., 2016, "Flutter suppression of plates subjected to supersonic flow using passive constrained viscoelastic layers and Golla–Hughes–McTavish method," Aerospace Science and Technology, **52**, pp. 70–80.

[23] Martins, P. C., Guimarães, T. A., Pereira, D. d. A., Marques, F. D., and Rade, D. A., 2017, "Numerical and experimental investigation of aeroviscoelastic systems," Mechanical Systems and Signal Processing, **85**, pp. 680–697.

[24] Martins, P. C., De Paula, A. S., Carneiro, S. H., and Rade, D. A., 2022, "Hybrid control technique applied to an aero-servo-viscoelastic simplified wing model," Aerospace Science and Technology, **122**, p. 107387.

[25] Liu, Q., Xu, Y., and Kurths, J., 2018, "Active vibration suppression of a novel airfoil model with fractional order viscoelastic constitutive relationship," Journal of Sound and Vibration, **432**, pp. 50–64.

[26] Lacarbonara, W. and Cetraro, M., 2011, "Flutter Control of a Lifting Surface via Visco-Hysteretic Vibration Absorbers," International Journal of Aeronautical and Space Sciences, **12**(4), pp. 331–345.

[27] Liu, Q., Xu, Y., and Kurths, J., 2020, "Bistability and stochastic jumps in an airfoil system with viscoelastic material property and random fluctuations," Communications in Nonlinear Science and Numerical Simulation, **84**, p. 105184.

[28] Sales, T., Marques, F. D., Pereira, D. A., and Rade, D. A., 2018, "Dynamic assessment of nonlinear typical section aeroviscoelastic systems using fractional derivative-based viscoelastic model," Journal of Sound and Vibration, **423**, pp. 230–245.

[29] Sales, T. d. P., Pereira, D. A., Marques, F. D., and Rade, D. A., 2019, "Modeling and dynamic characterization of nonlinear non-smooth aeroviscoelastic systems," Mechanical Systems and Signal Processing, **116**, pp. 900–915.

[30] Tian, H., Shan, X., Cao, H., Song, R., and Xie, T., 2021, "A method for investigating aerodynamic load models of piezoaeroelastic energy harvester," Journal of Sound and Vibration, **502**, p. 116084.

[31] Tian, H., Shan, X., Cao, H., and Xie, T., 2022, "Enhanced performance of airfoil-based piezoaeroelastic energy harvester: numerical simulation and experimental verification," Mechanical Systems and Signal Processing, **162**, p. 108065.

[32] Cunha-Filho, A., Briend, Y., de Lima, A., and Donadon, M., 2021, "A new and efficient constitutive model based on fractional time derivatives for transient analyses of viscoelastic systems," Mechanical Systems and Signal Processing, **146**, p. 107042.

[33] Erturk, A. and Inman, D. J., 2011, *Piezoelectric Energy Harvesting*, Wiley.

[34] Theodorsen, T., 1935, "General Theory of Aerodynamic Instability and the Mechanism of Flutter NTRS Document, NACA-TR-496." NACA, https://ntrs.nasa.gov/citations/19930090935

[35] Bisplinghoff, R. L. and Ashley, H., 1975, *Principles of Aeroelasticity*, Dover Publications, Inc, New York, NY.

[36] Vasconcellos, R., Abdelkefi, A., Marques, F., and Hajj, M., 2012, "Representation and analysis of control surface freeplay nonlinearity," Journal of Fluids and Structures, **31**, pp. 79–91.

[37] Khatua, T. P. and Cheung, Y. K., 1973, "Bending and vibration of multilayer sandwich beams and plates," International Journal for Numerical Methods in Engineering, **6**(1), pp. 11–24.

[38] Rao, S. S., 2010, *Mechanical Vibrations*, 5th ed., Pearson.

[39] Cunha Filho, A., 2019, "Abordagem transiente sobre os efeitos do amortecimento viscoelástico na estabilidade aeroelástica de estruturas aeronáuticas," Ph.D. thesis, Universidade Federal de Uberlândia, doi: 10.14393/ufu.te.2019.2208, https://repositorio.ufu.br/handle/123456789/28227

[40] Tian, W., Yang, Z., and Gu, Y., 2017, "Dynamic analysis of an aeroelastic airfoil with freeplay nonlinearity by precise integration method based on Padé approximation," Nonlinear Dynamics, **89**(3), pp. 2173–2194.